J Mater Sci (2006) 41:4434–4439
DOI 10.1007/s10853-006-0083-y

HRTEM investigation of the epitaxial growth of scandate/titanate multilayers

Markus Boese · Tassilo Heeg · Jürgen Schubert · Martina Luysberg

Received: 9 January 2006 / Accepted: 13 March 2006 / Published online: 28 June 2006

Abstract Despite their potential application in strain-engineered layer structures, the epitaxial growth of rare earth scandate films on cubic perovskite substrates is not fully understood to date. Here we report on the epitaxy of the orthorhombic $GdScO_3$ and $DyScO_3$ on (001) $BaTiO_3$ and $SrTiO_3$ thin films. In particular, the orientation relationship between the orthorhombic epilayer and the cubic substrate is examined by aberration corrected high-resolution transmission electron microscopy. For all cases investigated, the long axis of the orthorhombic unit cell was found to be perpendicular to the growth direction.

Introduction

The technological interest in rare earth scandates ($REScO_3$, RE = rare earth element) is twofold. First, the large dielectric constant and the large optical bandgap make the rare earth scandates promising candidates for the replacement of conventional gate oxide materials in MOSFET devices [1]. This is of particular interest regarding the further miniaturization of Si-based MOSFETs, which requires the replacement of the prevalent silicon oxynitrides by high-k materials. Here, the thermodynamic stability of the rare earth scandates against silicon is of advantage, too. Second, rare earth scandates have a large potential to serve as substrate material for the epitaxial growth of perovskites [2]. As a result of the large range of available lattice constants, depending on the composition of the substrate, different strain situations within the epitaxial films could be realized [3]. This strain engineering of earth alkali titanate layers allows tuning of their dielectric properties. For instance, for $BaTiO_3$ (BTO) grown onto $GdScO_3$ (GSO) the dielectric constant of the compressively strained titanate is three times larger compared to the bulk material [4]. By depositing $SrTiO_3$ (STO) on a $DyScO_3$ (DSO) substrate the epilayer becomes tensilely strained and thereby room temperature ferroelectricity is achieved [5].

Most of the $REScO_3$ compounds adopt the orthorhombic $GdFeO_3$-structure at room temperature [6], which can be described by the Pnma space group. This geometry results from a distorted cubic perovskite structure. The parameters a, b and c of the orthorhombic lattice are related to the lattice constant a_p of the cubic perovskites: $a \approx a_p\sqrt{2}$, $b = 2a_p$, and $c \approx a_p\sqrt{2}$. The pseudocubic lattice constant a_p varies between 0.394 nm and 0.405 nm depending on the rare earth element chosen.

The symmetry break with respect to the orthorhombic structure from the cubic ABO_3 structure can be ascribed to tilted BO_6 octahedra. These tilts cause an anisotropy of the dielectric constant [7]. For $DyScO_3$ the dielectric constant differs by a factor of two. The largest value is observed along the longer axis in the orthorhombic unit cell [8] (for space group Pnma, this is the b axis).

Several perovskite-based thin films with $GdFeO_3$-structure, which were epitaxially grown on perovskite substrates, have been investigated so far. For $SrRuO_3$ [9] and several manganate perovskites [10–12] the long b axis was predominantly found within the film plane. However, two orientation relationships mutually rotated by 90°

M. Boese (✉) · M. Luysberg
Institut für Festkörperforschung and Ernst Ruska-Centrum für Mikroskopie und Spektroskopie mit Elektronen, Forschungszentrum Jülich, 52425 Jülich, Germany
e-mail: m.boese@fz-juelich.de

T. Heeg · J. Schubert
Institut für Schichten und Grenzflächen, Forschungszentrum Jülich, 52425 Jülich, Germany

around the normal of the substrate were reported, resulting in a domain structure. The magnetic anisotropy is strongly affected by the occurrence of these domains [13]. Making use of the anisotropic, magnetic or, in our case, dielectric properties the understanding of the epitaxial growth is required, in particular regarding the orientation relationships.

In our paper we employ aberration-corrected transmission electron microscopy to determine the atomic structure of $GdScO_3$ and $DyScO_3$ films and their epitaxial relationship within $GdScO_3/BaTiO_3$ and $DyScO_3/SrTiO_3$ multilayers. Avoiding aberrations is necessary to distinguish between slightly different contrast features of the scandate and titanate perovskite structures.

Experimental

Multilayers of $GdScO_3/BaTiO_3$ and $DyScO_3/SrTiO_3$ were deposited on $SrTiO_3$ (100) substrates covered with a 150-nm thick $SrRuO_3$ buffer layer. Both, the $SrRuO_3$ electrode and the multilayer system were grown by pulsed laser deposition (PLD) at a substrate temperature of 650–700 °C. The multi-layered stack consists of 20 double layers of scandate/titanate. Rutherford backscattering spectrometry revealed a thickness of 100 nm of the stack. The $BaTiO_3/GdScO_3$ multilayer system exhibits a dielectric constant ϵ_r of 60 at 1 MHz. Details of the growth procedure and electrical measurement are described elsewere [14]. Different strain situations are realized for the multilayers grown on the SrRuO3 electrode. Whereas a tensile strain can be assumed for $BaTiO_3$ in the $GdScO_3/BaTiO_3$ multilayers, a compressive strain is applied to SrTiO3 in the $DyScO_3/SrTiO_3$ system. For comparison the lattice parameter of the deposited layers are given in Table 1.

Cross-sectional samples for TEM investigation were obtained by mechanical preparation down to a thickness of 20 μm followed by Ar ion milling (Technoorg LINDA). Initially an Ar energy of 5 kV was employed. Clean surfaces were achieved by a final treatment with 0.5 kV Argon ions.

Aberration-corrected high-resolution transmission electron microscopy was carried out with a negative spherical-aberration value (C_s) of −40 μm in a Philips CM200/FEG at 200 kV equipped with a CEOS double hexapole corrector. Choosing the optimum overfocus setting of the objective lens of 12 nm results in a directly interpretable bright atom contrast and in a minimized sub-Ångstrom delocalisation [15]. Prior to image acquisition the aberrations were evaluated and adjusted using Zemlin tableaus [16]. The minimization of the lens aberrations was accomplished by adjusting the appropriate lens currents of the C_s correction system. Focus series were recorded and, subsequently, the exit-plane wave was reconstructed using the ''True Image'' software (FEI), which is based on the Philips-Brite-Euram software package [17, 18]. Residual aberrations were numerically corrected for the complex-valued exit-plane wave. A combination of hardware spherical aberration correction and numerical phase retrieval methods is used to take advantage of both methods. Imaging at a negative C_s value yields an enhanced bright atom contrast [15]. Due to practical issues, e.g., instabilities of the specimen, aberrations like two-fold astigmatism or coma are frequently present during image acquisition. The focus series reconstruction (FSR) of the exit-plane wavefunction enables an a posteriori fine-tuning of residual aberrations. This method provides contrast enhancement of weak features (oxygen sublattice) and an improvement of the signal-to-noise ratio. During focus series acquisition stable conditions are required for at least one minute. If this is not fulfilled almost directly interpretable images with low residual aberrations can be used. The EMS software package [19] and MacTempas [20] were applied to numerically simulate the exit-plane wave and the high-resolution images. Supercells of the scandate/titanate interface were generated as input for the multislice calculations. Supercells were constructed using the software ''CrystalKit'' (Total Resolution) implying the lattice parameters reported in literature. An overview of the crystal data is given in Table 1.

Results and discussion

Bright-field imaging and electron diffraction

An overview micrograph of the entire thin-film stack is given in Fig. 1. Both, the $SrRuO_3$ electrode and the

Table 1 Bulk lattice parameters of the scandates (orthorhombic), $SrRuO_3$ (orthorhombic), $SrTiO_3$ (cubic) and BaTiO3 (tetragonal)

	a (nm)	b (nm)	c (nm)	a_p (nm)	Reference
$GdScO_3$	0.5486	0.7934	0.5750	≈0.397	[6]
$DyScO_3$	0.5449	0.7931	0.5726	≈0.395	[6]
$SrRuO_3$	0.5564	0.7843	0.5530	≈0.392	[21]
$SrTiO_3$ (cubic)	0.3905				[22]
$BaTiO_3$ (tetragonal)	0.3997		0.4031		[23]

Pseudocubic lattice constant a_p is given for comparison of the orthorhombic structures with the titanates

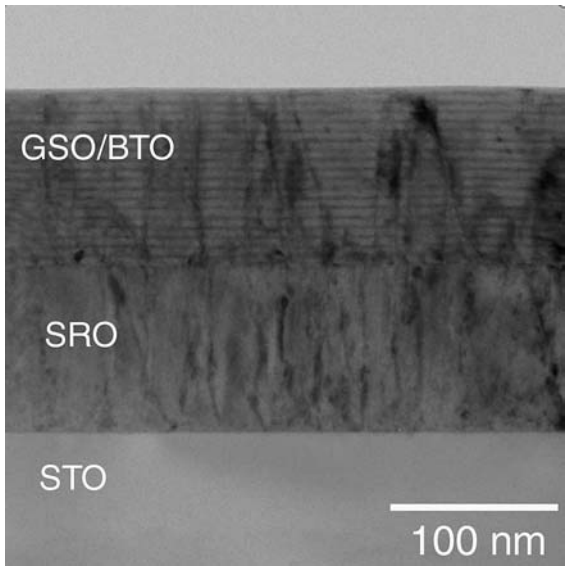

Fig. 1 Bright-field image of $GdScO_3/BaTiO_3$ multilayers grown on $SrRuO_3$-buffered $SrTiO_3$ substrate

multilayer stack are 110 nm thick. Misfit dislocations are observed at the interface between the $SrRuO_3$ buffer and the $SrTiO_3$ substrate, indicating that the lattice mismatch between $SrRuO_3$ buffer and substrate is at least partially relaxed. This is in agreement with literature, where relaxation of $SrRuO_3$ film is reported to occur already at thicknesses larger than 35 nm [24]. Dark Bragg contrasts aligned in growth direction are identified as threading dislocations. These dislocations are spread into the multilayer film. The multilayered stack can be easily distinguished from the $SrRuO_3$. The appearance of darker lines perpendicular to the growth direction is due to the stronger electron diffraction at the heavier element gadolinium.

The electron diffraction pattern of the multilayered stack is shown in Fig. 2. The strong diffraction spots arranged in a quadratic pattern coincide with the reflections of the $BaTiO_3$ layers in the $[100]_{BTO}$ zone axis and with the reflections of both $GdScO_3$ variants, i.e. the $[101]_{GSO}$ zone axis and the $[010]_{GSO}$ zone axis. The schematic drawing in Fig. 2b shows the diffraction spots of both variants as crosses and circles, respectively. In addition to the strong diffraction spots, where the reflections of both variants and of the $BaTiO_3$ coincide, weak reflections are detected, which can be attributed to the orthorhombic structure of the $GdScO_3$ layers. The individual strong reflections are decorated by satellites which arise from the superlattice. The size of one double layer measured from the separation of the satellite spots is 5.6 ± 0.5 nm. An identification of the difference in the lattice parameters of the $BaTiO_3$ and $GdScO_3$ layers is hampered by the occurrence of satellite spots.

From the analysis of the diffraction pattern two orientation relationships between the $BaTiO_3$ and $GdScO_3$ layers are evident. These relationships are schematically shown in Fig. 3. In the case of variant I the $[101]_{GSO}$ direction is aligned parallel to the $[100]_{BTO}$ direction, whereas in variant II it is rotated by 90° with respect to variant I around the growth direction. Both variants have in common that the longer *b*-axis of the orthorhombic $GdScO_3$ is located in the growth plane.

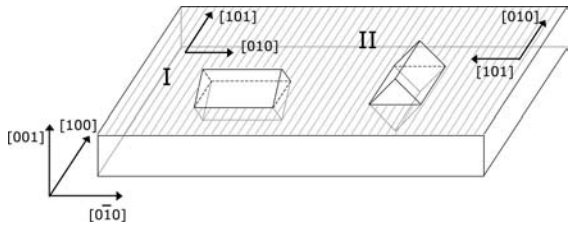

Fig. 3 The two orientation variants observed in $GdScO_3$ (and $DyScO_3$). For each variant the orientation of the orthorhombic unit cell is shown and the crystallographic directions are indicated accordingly. The hatched plane denotes a (001) plane of the $BaTiO_3$ ($SrTiO_3$) layers

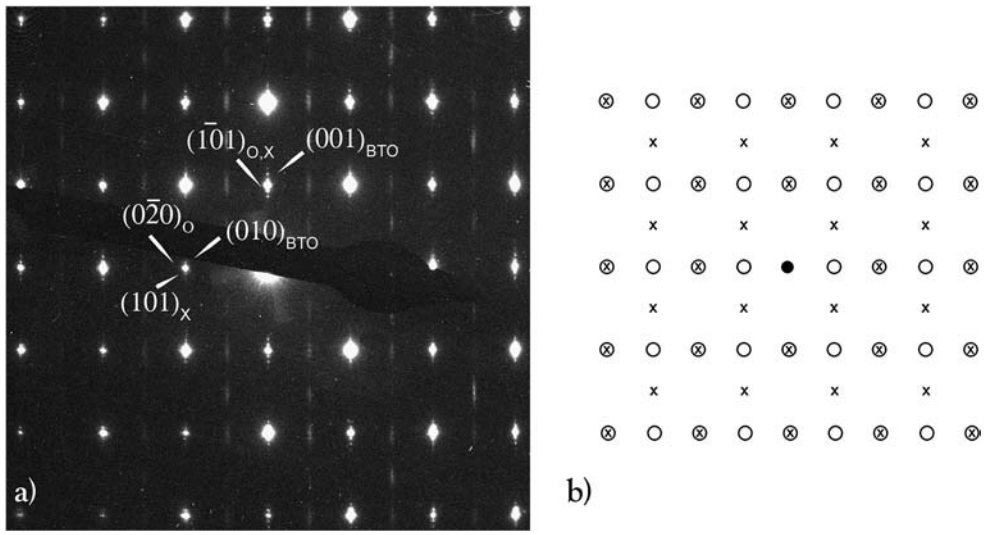

Fig. 2 (**a**) Selected-area diffraction pattern of the $GdScO_3/BaTiO_3$ double layers with reflections of $GdScO_3$ viewed along the [101] zone axis (O) and $GdScO_3$ viewed along the [010] zone axis (X). The $BaTiO_3$ zone axis is indexed as [100]. (**b**) Schematic electron diffraction pattern of $GdScO_3$ viewed along the [101] and [010] zone axes marked by O and X, respectively. The $BaTiO_3$ reflections are coincident with the superposed reflections of the two orientation variants of $GdScO_3$

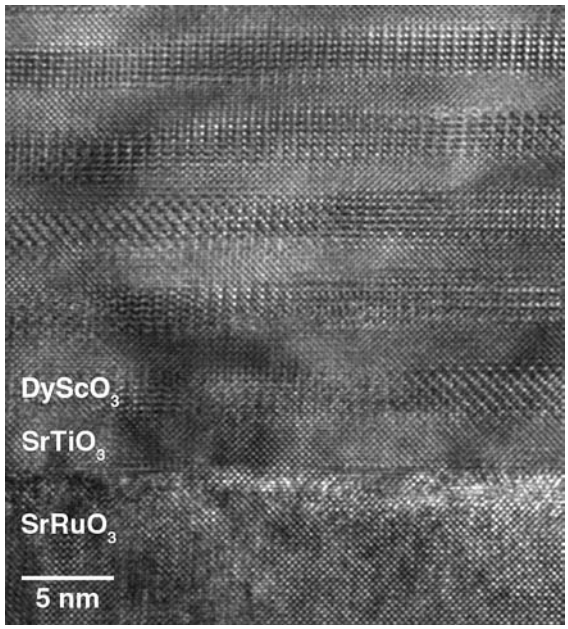

Fig. 4 High-resolution lattice fringe image of $DyScO_3/SrTiO_3$ multilayers grown on $SrRuO_3$-buffered $SrTiO_3$ substrate

For the $DyScO_3/SrTiO_3$ multilayer system similar diffraction patterns are observed (not shown), leading to an identical orientation relationship as in the $GdScO_3/BaTiO_3$ case. These results agree with studies of epitaxial $SrRuO_3$ thin films [9] and orthorhombic manganates [10–12].

HRTEM of $DyScO_3/SrTiO_3$ multilayers

In principle, domains of orientation variants I and II in the orthorhombic scandate layers can be localized by dark-field imaging using the weak reflections of the two orthorhombic orientation variants. However, dark-field imaging of such small dimensions, i.e. 3 nm, is difficult. In addition, the intensity of these reflections is too weak to obtain dark-field images within reasonable acquisition time (< 20 s). Therefore, high-resolution transmission electron microscopy (HRTEM) is employed to identify both orientation variants on a nanometer scale.

Figure 4 shows a HRTEM image of the $DyScO_3/SrTiO_3$ multilayers in a thicker specimen region. The ruthenate layer exhibits a roughness of a few nanometers. The double layers are also affected by this irregularity.

The HRTEM image displayed in Fig. 5a was acquired under negative C_s and overfocus conditions, where an optimum phase contrast is achieved [15]. The specimen thickness decreases from the left to the right associated with the wedge shape of the specimen edge. Contrast variations within one layer are caused by thickness variations of the thin foil. Almost directly interpretable bright atom contrast is seen in thicknesses below the extinction distance of the heavy atom columns. Due to the roughness of the $SrRuO_3$ electrode (see Fig. 4) the interfaces between the scandate and the titanate layers are not atomically flat. For this reason, a local distinction between the both perovskite structures is hardly possible. The layer thicknesses are approximately 7 unit cells of $SrTiO_3$ and 5–6 unit cells of $DyScO_3$. Two regions within the $DyScO_3$ layers, which are marked by frames within Fig. 5a, are displayed in Fig. 5b for closer inspection. The comparison between experimental and simulated image patterns yields a defocus of +8 nm and a specimen thickness of 4.5 nm. The experimental and simulated image of region I matches for the [101]-zone axis, which corresponds to the orientation variant I according to Fig. 3. In contrast, in region II the [010] direction is aligned parallel to the incident electron waves. In this orientation the Dy atoms are slightly displaced with respect to a straight column causing an elongation of the contrast dots associated with the Dy

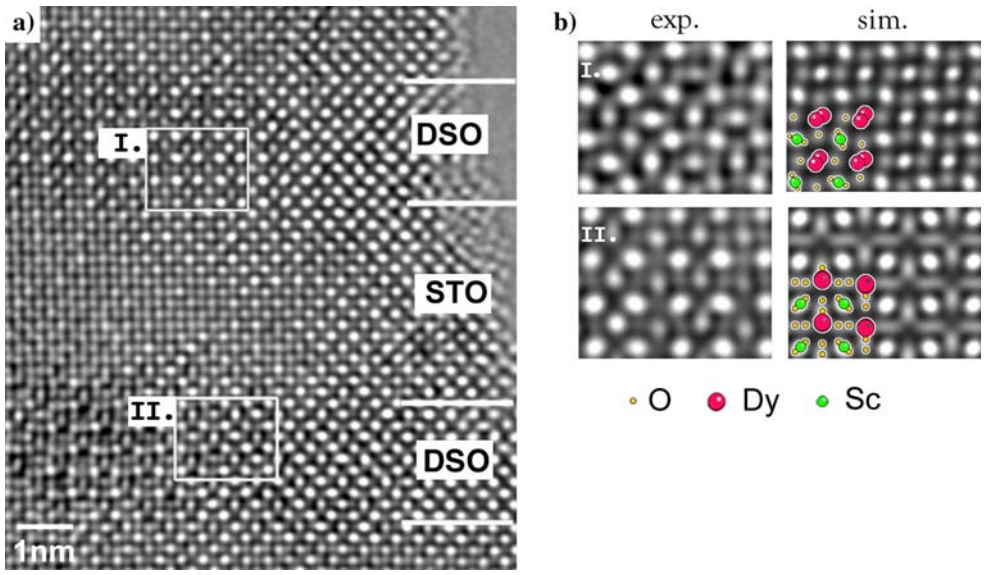

Fig. 5 (**a**) HRTEM image taken under negative spherical aberration imaging conditions showing nearly delocalisation free, almost directly interpretable images under bright atom contrast focus setting. (**b**) Comparison between experimental and simulated images on the left-hand side and on the right-hand side, respectively, for the orientation variants I: [101] zone axis, and II: [010] zone axis

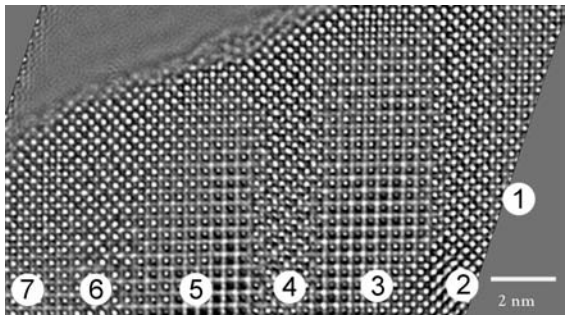

Fig. 6 Phase image of the reconstructed exit-plane wavefunction showing seven layers of $GdScO_3$ and $BaTiO_3$, growth direction from right to left. The zone axes are identified as: [100] $BaTiO_3$ layers 1,3,5 and 7; [101] $GdScO_3$ layer 2; [0 $\bar{1}$0] $GdScO_3$ layer 4; [010] $GdScO_3$ layer 6

columns. In contrast, within region I, Dy atoms are well aligned along a straight column. Hence, the extinction distance is decreased resulting in weaker contrast. For both orientation variants the Sc–O positions appear as elongated spots, reflecting the superposition of a scandium column with two neighbouring half occupied oxygen columns.

HRTEM of $GdScO_3/BaTiO_3$ multilayers

Exit-plane wave reconstruction [18] was utilized for the analysis of $GdScO_3/BaTiO_3$ multilayers a focus series of 20 images with a focal increment of −1.7 nm was recorded and the exit-plane wavefunction was reconstructed. The complex valued wave function was used for the a posterior fine-tuning of residual aberrations [25]. The phase image shown here is corrected by software for a two-fold astigmatism, A2 = 11.5 nm and a coma, B = 150 nm.

The phase image in Fig. 6 shows the alternating layers of the different perovskite structures. The interfaces appear sharp. A specimen thickness of 6.4 nm is estimated by comparison with calculated phase images of the wave function for one single $GdScO_3$ layer. The $BaTiO_3$ layers are approximately 5 nm thick. The different zone axes of $GdScO_3$ layers are identified by comparison with simulated exit-plane wavefunctions. Figure 7 displays a magnified view in combination with structure models and image simulations. The indicated unit cell axes of $GdScO_3$ (top left) clarify the direction of the *b*-axis. In agreement with the results obtained by electron diffraction, the *b*-axis was found perpendicular to the growth direction. Hence, only orientation variants I and II (see Fig. 3) were observed and are displayed in Fig. 7a and b, respectively.

In the case of orientation variant I, i.e. the [101] zone axis, the Gd columns are arranged in a zig-zag manner along the *b*-axis, which is indicated by the bright line. The Sc columns show a bright contrast dot, which is elongated due to the oxygen columns close by. The oxygen columns between the Gd positions result in a weaker contrast compared to the oxygen columns within the $BaTiO_3$. This

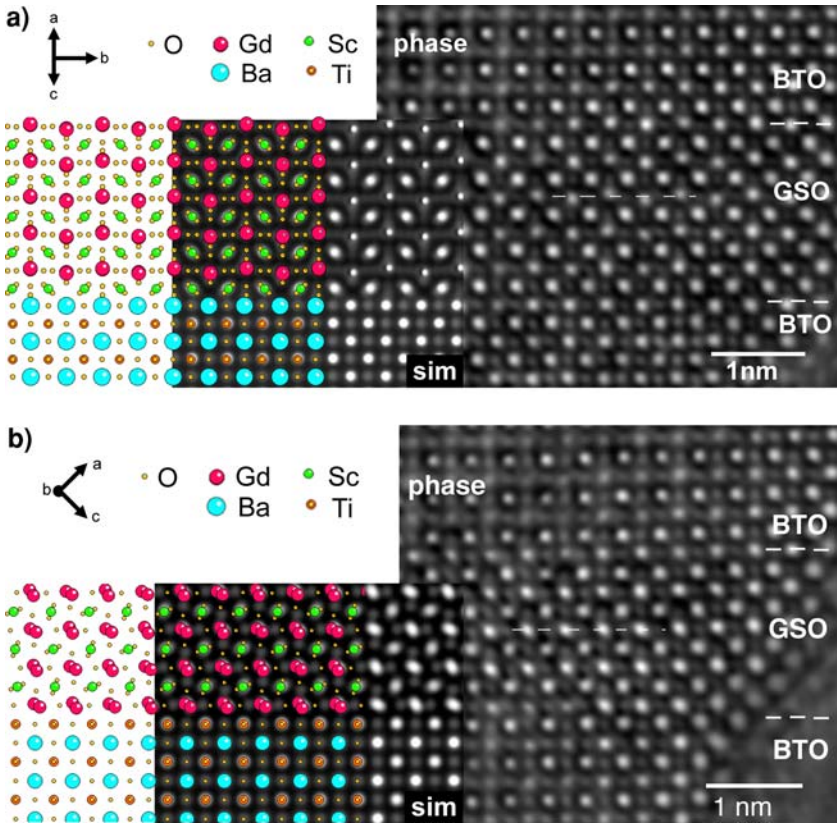

Fig. 7 (**a**) Phase image of $GdScO_3$ [101] (layer 2 in Fig. 7) in-between $BaTiO_3$ layers. (**b**) Phase image of $GdScO_3$ [010] (layer 4 in Fig. 7) in-between $BaTiO_3$ layers

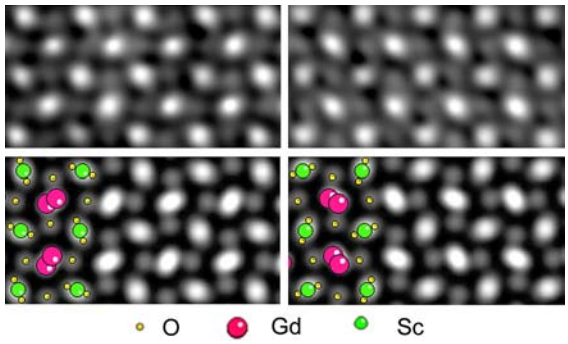

Fig. 8 $DyScO_3$ viewed along the [0 $\bar{1}$0] (left) and [010] (right) zone axes. Experimental images of layer 6 (left) and layer 4 (right) in Fig. 7 are compared to simulations (bottom)

reduced contrast is caused by the distorted perovskite structure resulting in two neighbouring oxygen columns, each of them 1/2 occupied. In contrast, the oxygen positions within the $GdScO_3$ layer with orientation variant II (Fig. 7b) show similarly strong contrast as within the $BaTiO_3$ layer. Here, the oxygen column is displaced as a whole. In this orientation both the Sc and the Gd columns are characterized by elongated spots according to the projected crystal structure.

The orientation relationship between $GdScO_3$ and the $BaTiO_3$ becomes unambiguous upon distinction between the 180° variants of the ⟨010⟩ zone axis of the $GdScO_3$, which is illustrated in Fig. 8. The scandate layer 6 in the [0$\bar{1}$0] orientation and layer 4 on the [010] zone axis are displayed. The elongation of the spots is caused by a structural inherent displacement of Gd atoms from columnar positions. This contrast feature appearing in the phase image makes the identification of the particular zone axis possible.

Conclusion

Aberration-corrected high-resolution electron microscopy and numerical phase retrieval methods were successfully applied to identify the orientation relationship between rare earth scandate and titanate layers. For all $DyScO_3$ and $GdScO_3$ layers grown onto (100) titanates only two orientation variants have been observed: the [101] and [010] zone axes. Thus, the *b* axis of the orthorhombic scandate unit cell is always aligned perpendicular to the growth direction, which is also confirmed by electron diffraction. These orientation relationships, which were also reported for manganites [10–12] and ruthenates [9], seem to be common for the epitaxial growth of orthorhombic onto cubic perovskites.

Acknowledgements Fruitful discussions with L. Houben and C. L. Jia are gratefully acknowledged. We are thankful to D. Meertens for support with the specimen preparation. T.H. gratefully acknowledges financial support of the Deutsche Forschungsgemeinschaft, Graduiertenkolleg 549 'Noncentrosymetric Crystals'.

References

1. Schlom DG, Haeni JH (2002) Mater Res Soc Bull 27:198
2. Schubert J, Trithaveesak O, Petraru A, Jia CL, Uecker R, Reiche P, Schlom DG (2003) Appl Phys Lett 82:3460
3. Shin-Ichi K, Naito M (2004) Appl Phys Lett 84:2136
4. Choi KJ, Biegalski M, Li YL, Sharan A, Schubert J, Uecker R, Reiche P, Chen YB, Pan XQ, Gopalan V, Chen L-Q, Schlom DG, Eom CB (2004) Science 306:1005
5. Haeni JH, Irvin P, Chang W, Uecker R, Reiche P, Li YL, Choudhury S, Tian W, Hawley ME, Craigo B, Tagantsev AK, Pan XQ, Streiffer SK, Chen LQ, Kirchoefer SW, Levy J, Schlom DG (2004) Nature 430:758
6. Liferovich RP, Mitchell RH (2004) J Solid State Chem 177:2188
7. Valant M, Suvorov D, Rawn CJ (1999) Jpn J Appl Phys 38:2820
8. Chang W, Kirchoefer SW, Bellotti JA, Qadri SB, Pond JM, Haeni JH, Schlom DG (2004) J Appl Phys 96:6629
9. Jiang JC, Pan QX, Chen CL (1998) Appl Phys Lett 72:909
10. Ma XL, Zhu YL, Meng XM, Lu HB, Chen F, Chen ZH, Yang GZ, Zhang Z (2002) Phil Mag A 82:1331
11. Lu CJ, Wang ZL, Xiong GC, Lian GJ (2000) J Mater Res 15:2454
12. Zhu YL, Ma XL, Li DX, Lu HB, Chen ZH, Yang GZ (2003) Phys Stat Sol 199:233
13. Wang HS, Li Q, Liu K, Chien CL (1999) Appl Phys Lett 74:2212
14. Heeg T, Wagner M, Schubert J, Buchal CH, Boese M, Luysberg M, Cicerrella E, Freeouf JL (2005) Microelectron Eng 80:150
15. Lentzen M (2004) Ultramicroscopy 99:211
16. Uhlemann S, Haider M (1998) Ultramicroscopy 72:109
17. Coene WMJ, Thust A, Op De Beeck M, Van Dyck D (1996) Ultramicroscopy 64:109
18. Thust A, Coene WMJ, Op De Beeck M, Van Dyck D (1996) Ultramicroscopy 64:211
19. Stadelmann PA (1987) Ultramicroscopy 21:131
20. Kilaas R (1987) In: Bailey GW (ed) Proceedings of the 45th annual EMSA meeting. San Francisco Press, San Francisco, CA, pp 66–67
21. Gardener JS, Balakrishnan G, Mck. Paul D (1995) Physica C 252:303
22. Besch W, Schmalle HW, Reller A (1990) Solid State Ionics 43:171
23. Kwei GH, Lawson AC, Billinge SJL, Cheong S-W (1993) J Phys Chem 97:2368
24. Ban Z-G, Alpay SP, He F, Wells BO, Xi XX (2004) Appl Phys Lett 84:4848
25. Thust A, Overwijk MHF, Coene WMJ, Lentzen M (1996) Ultramicroscopy 64:249